Volume 7 Number 2 Apr - Jun 2018

STUDENT JOURNAL OF PHYSICS

INTERNATIONAL EDITION

INDIAN ASSOCIATION OF PHYSICS TEACHERS

ISSN – 2319-3166

STUDENT JOURNAL OF PHYSICS

This is a quarterly journal published by Indian Association Of Physics Teachers. It publishes research articles contributed by Under Graduate and Post Graduate students of colleges, universities and similar teaching institutions, as principal authors.

Registered Office

Editor-in-Chief, SJP, Institute of Physics, Sainik School, Bhubaneswar, Odisha, India – 751005
(www.iopb.res.in/~sjp/)

STUDENT JOURNAL OF PHYSICS

Scope of the Journal

The journal is devoted to research carried out by students at undergraduate level. It provides a platform for the young students to explore their creativity, originality, and independence in terms of research articles which may be written in collaboration with senior scientist(s), but with a very significant contribution from the student. The articles will be judged for suitability of publication in the following two broad categories:

1. **Project based articles**
   These articles are based on research projects assigned and guided by senior scientist(s) and carried out predominantly or entirely by the student.
2. **Articles based on original ideas of student**
   These articles are originated by the student and developed by him/ her with possible help from senior advisor. Very often an undergraduate student producing original idea is unable to find a venue for its expression where it can get due attention. SJP, with its primary goal of encouraging original research at the undergraduate level provides a platform for bringing out such research works.
   It is an online journal with no cost to the author.

Since SJP is concerned with undergraduate physics education, it will occasionally also publish articles on science education written by senior physicists.

Information for Authors

- Check the accuracy of your references.
- Include the complete source information for any references cited in the abstract. (Do not cite reference numbers in the abstract.)
- Number references in text consecutively, starting with [1].

- Language: Papers should have a clear presentation written in good English. Use a spell checker.

Submission

1. Use the link "Submit" of Website to submit all files (manuscript and figures) together in the submission (either as a single .tar file or as multiple files)
2. Choose one of the Editors in the link "Submit" of Website as communicating editor while submitting your manuscript.

Preparation for Submission

Use the template available at "Submit" section of Website for preparation of the manuscript.

Re-Submission

- For re-submission, please respond to the major points of the criticism raised by the referees.
- If your paper is accepted, please check the proofs carefully.

Scope

- SJP covers all areas of applied, fundamental, and interdisciplinary physics research.

STUDENT JOURNAL OF PHYSICS

Multiphysics Design of the Double Quarter-Wave Resonator Separator

David Diaz[1], Alexander Plastun[2], Peter Ostroumov[3]

[1]Third Year Undergraduate (junior), Department of Physics, Stony Brook University, Stony Brook, NY, 11794

[2]Accelerator Physicist, Accelerator Systems Division, Accelerator Physics Department, Facility for Rare Isotope Beams, Michigan State University, East Lansing MI, 48824

[3]Accelerator Physics Department Manager, Accelerator Systems Division, Accelerator Physics Department, Facility for Rare Isotope Beams, Michigan State University, East Lansing MI, 48824

Abstract: The Facility for Rare Isotope Beams and its experimental systems are currently under construction. The RF deflector based on a Double Quarter-Wave Resonator (QWR) is being designed for separation of rare isotopes. This paper presents some aspects of a multiphysics design of the RF deflector. The resonator will consume 42 kW RF power in order to provide the required deflection of ion beams. Removal of the heat from the resonator is required to control its shape and dimensions since the resonator should always be in resonance with the beam. The resonator is supported by a six-strut system to minimize the offset between the resonator and beam axes. Two cooling design options of heat pipes were also implemented into the resonator electrodes to improve the heat flow and temperature distribution. The rest change in resonant frequency due to thermal expansion will be corrected by using tuners.

Keywords: FRIB, RF Deflector, Surface Currents, Thermal Expansion

1. INTRODUCTION

The Facility for Rare Isotope Beams (FRIB) is currently being constructed at Michigan State University and will replace the existing Coupled Cyclotron Facility [1]. The experimental systems of the facility are being upgraded. One of the experimental beamlines will be equipped with an RF deflector for separation of the rare isotope beam. The RF deflector is based on the Double Quarter-Wave Resonator (QWR), Figure 1. The electromagnetic field excited inside the cavity resonator creates surface currents which lead to RF power dissipation and temperature increase of the cavity electrodes. This increase in temperature causes thermal expansion which alters the geometry of the magnetic and electric fields.

diaz_davido@hotmail.com[1], plastun@frib.msu.edu[2], ostroumo@frib.msu.edu[3]

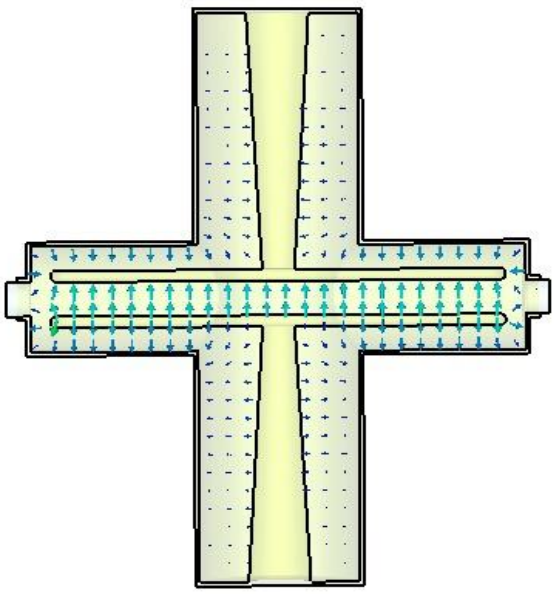

Figure 1. A cross section of the initial design for the QWR before any hermal management systems and nechanical supports are implemented. Here the electric field lines are being shown. The electric field that is produced in between the electrodes, capacitors, are due to the surface currents that are created when the cavity is in resonance. A magnetic field s also produced on the upper and ower parts of the cavity around the nner stems. The cavity is 3 meters high and 2.6 meters long.

Here is a way to understand the relation with resonance frequency change [2]:

$$\frac{\omega-\omega_0}{\omega_0}=\frac{\Delta U_m-\Delta U_e}{U_m+U_e} \tag{1}$$

where ω_0 is the initial resonance frequency of the unperturbed cavity, ω is the resonance frequency of the deformed cavity, U_m is the stored magnetic energy, and U_e is the stored electric energy. Eq. (1) shows how the change in magnetic and electric field energies are related to the change in resonance frequency. Creating the thermal management and mechanical support of the cavity would minimize the effects of thermal expansion and the optical axis offset. The following three equations show how thermal expansion affects the stored magnetic and electric energies:

$$\Delta L=L_0\alpha\Delta T \tag{2}$$

ΔL is the linear change in length of the electrodes and stems due to thermal expansion, L_0 is the original length of the material, α is the expansion coefficient of the material, and ΔT is the change in temperature of the material [3].

$$U_e=\frac{1}{2}\frac{\epsilon_0 A}{d}V^2=\frac{1}{2}CV^2, \tag{3}$$

where ϵ_0 is the permeability of free space, A is the planar surface area of each capacitor, d is the space in between the capacitors, C is the capacitance and V is the voltage [4].

(4)

$$U_m = \frac{B^2}{2\mu_0} AL,$$

Where μ_0 is the permittivity of free space, A is the cross-sectional area of the inductor, which is the stem, and L is the inductance [5].

The stored magnetic energy of the cavity is represented as an inductance because cavities can be modeled as RLC circuits. This specific cavity follows the path in Figure 2, where C_1 and C_2 are the capacitance between the electrodes and the tank, C_{coup} is the coupled capacitance between the electrodes, L_1 and L_2 are the equivalent inductance of the stems, and L_{coup} is the coupled inductance representing the current flow from one-half of the cavity to the other. You can see the circuit illustration of the QWR in Figure 2 below.

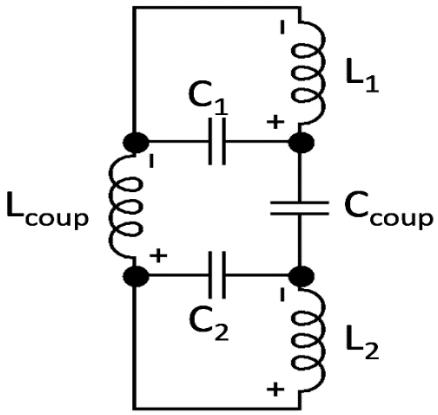

Figure 2. This is a sketch of the circuit representation of the double quarter wave resonator. Since, the cavity is able to be modeled in such a way, equations (2), (3), and (4) are sufficient enough to determine the change in resonance using equation (1).

2. DOUBLE QUARTER-WAVE RESONATOR SEPARATOR

The QWR is supposed to perform as an ion separator because of the RF electric field that is created in between the capacitors and oscillates at 20.125 MHz, Figure 1. The surface currents that are created go from one capacitor plate, up through its stem and around the cavity to the opposite stem and another capacitor plate. This path alternates in direction and so does the electric and magnetic fields. When an ion goes through the cavity, the electric field moves the ion in the ± $y^{¿}$ depending on its mass and RF phase. Plot 1 shows an example of $^{100}Sn^{50+}$ going through the cavity at the kinetic energy of 100 MeV/u, which results in an offset of approximately 14 mm near the end plane. This separation is important because a beam can contain many different particles and this will allow the separation of the beam depending on their arrival time to the cavity. Slits will be placed downstream the cavity to improve the purity of the beam. This ion motion simulation was performed with CST Particle Studio [6].

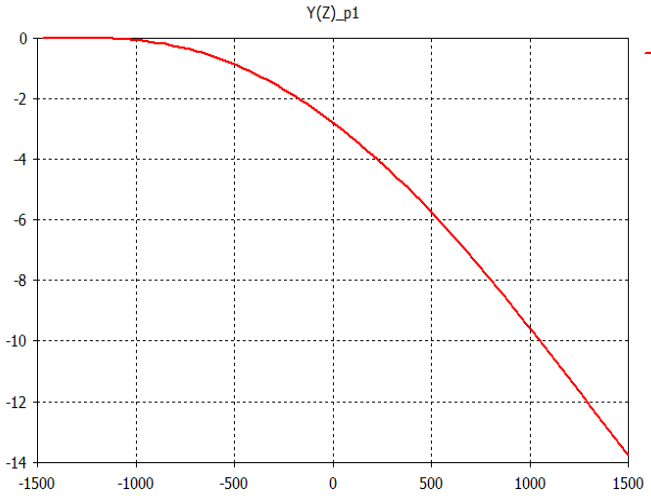

Plot 1. This is an example of $^{100}Sn^{50+}$ going through the cavity and acquiring an offset of approximately 14 mm from the optical axis. Both axes have the unit of mm and the cavity starts and ends at 1300 mm, respectively.

3. MULTIPHYSICS DESIGN

In order to minimize the thermal expansion, the temperature of the cavity needs to decrease. I used different approaches to cool the cavity. Different sections of the cavities produce different thermal losses, so the amount of cooling that is required can vary amongst different sections of the cavity. From the Thermal Solver in CST, I was able to determine the thermal losses in units of W/m^2, so to determine the overall thermal losses, I calculated the surface area of each section, i.e. stem, capacitor, and bases, and multiplied it by its average thermal loss in units of W/m^2.

The following table shows the power loss per section of the cavity:

Section	Units	Value
Top/Bottom Base	[W]	1333.5
Stem	[W]	14231.1
Top/Bottom Cylinder	[W]	3427.8
Top Part of Capacitor	[W]	1315.7
Bottom Part of Capacitor	[W]	218.4

Table 1. This shows the average values of thermal losses in the cavity due to resonance. The “Top Part” of the capacitor refers to the face that is farthest from the beam axis and the “Bottom Part” refers to the closest face.

The thermal losses shown in Table 1, drastically increase the temperature of the cavity, so the cooling channels and heat pipes were implemented.

3.1 Cooling Channels

The cooling channels on the outer tank surfaces all have a semi-circular cross section with a radius of 10 mm and a hydraulic diameter of 12.2 mm. These channels contain a water velocity of 1.0 m/s and a convection coefficient (h) of approximately 4500 W/m^2•K. The velocity can be adjusted to reach differing h values and change temperature distribution. All the helical and spiral cooling channels are represented as rings in the simulation to improve simulation speeds. This was also done to incorporate different reference temperatures to each ring to represent the water temperature increase along the channels, which makes the simulations more accurate.

The cooling channels in the stem are helical with a rectangular cross section of 10 mm x 10 mm and a pitch of 20 mm. The helical section of the cooling channel provides the most cooling to the stem, while the inner cylindrical channel, radius of 5 mm, is mainly for the entrance of the water flow. The water velocity is 2.5 m/s and it provides a convection coefficient of approximately 9000 W/m^2•K.

3.2 Heat Pipes

Not adding any thermal management to the capacitors’ plates proved to be very undesirable since a temperature gradient of 70 K is produced on the capacitors. Cooling channels were considered to thermally manage the capacitors. Simulating cooling channels in the capacitors provided a temperature distribution of less than 1 K in the capacitors, which would be ideal.

However, manufacturing of these cooling channels in the capacitors would be too difficult to make watertight while minimizing distortions on the surface of the capacitors. For this reason, I looked into heat pipes to see if these devices would be able to cool the capacitors. Heat pipes are used in many systems as thermal management and provides a watertight passive process, which would require less maintenance in the long run. Heat pipes have been used to improve the temperature distribution and heat flow in the capacitors. They are used to cause a temperature distribution of 2-5 K and have thermal conductivity that range from ten times to ten thousand times the thermal conductivity of copper [7]. Heat pipes are made out of a metallic shell, a complimentary liquid, a wick structure and a vapor space. They use the phase changes of condensing and vaporizing to cause an increase in the pipe's effective thermal conductivity. This is done by gaining energy to vaporize at the evaporator section and then release that as latent heat at the condenser section. The wick structure in the heat pipes allows for capillary movement of the liquid in the pipe to move from the condenser section to the evaporator section. These wick structures are made out of grooved edges in metal or with sintered metal. The following figure is a diagram to help visualize how a heat pipe functions:

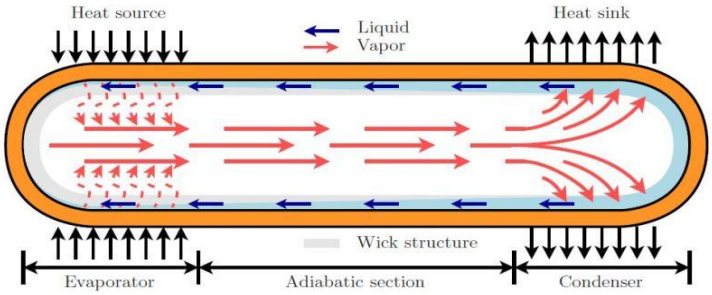

Figure 3. [8] This is a visual representation on the mechanics of a heat pipe as discussed in the text.

There are two designs for heat pipes in the capacitors with each heat pipe being cylindrical and encased in a 5 mm thick insulator, which can be seen in Figure 4. The insulator allows for 10 mm to be exposed on the condenser and evaporator sections of each heat pipe. The first design contains two sets of three parallel heat pipes, each 375 mm long, at each end of each capacitor, with the heat pipes closer to the stem being thicker due to the higher amount of heat flow. Heat pipes closer to the stem have a radius of 15.0 mm and the ones farther from the stem have a radius of 7.5 mm. The second design contains a set of three parallel heat pipes at each end of each capacitor with each pipe having a radius of 15.0 mm, but the center heat pipe would have a length of 800 mm and the ones on the sides would have a length of 400 m.

These designs were created to maximize heat flow and minimize the temperature distribution while maintaining more of a uniform distribution as opposed to having undesirable peaks.

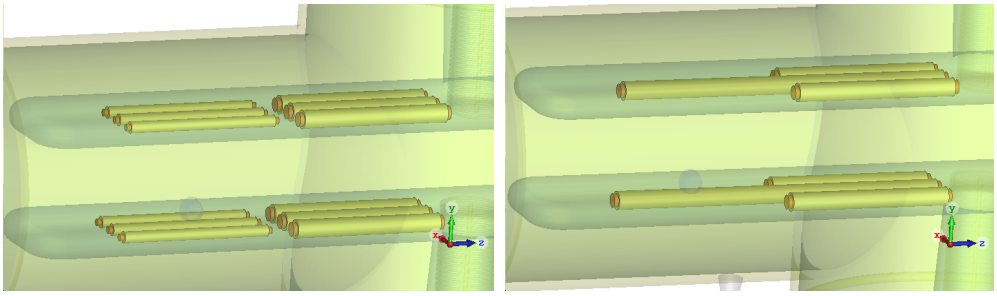

Figure 4. The left figure shows the first design of heat pipes that contains two sets of three parallel heat pipes partially surrounded by insulation. The right figure shows the second design of three parallel heat pipes of different sizes partially surrounded by insulation.

The heat pipes were simulated by creating a material similar to copper, except for its thermal conductivity which was varied to determine the right conductivity to create an accurate temperature distribution. After determining the thermal conductivity that creates a temperature distribution of 2-5 K, one has to check the power flow in the design center of Thermacore to see the limitations. This is done by noting the maximum and minimum heat flow that would be associated with each thermal conductivity. For the first design, the heat pipes closer to the stem had a thermal conductivity of 40,000 W/m·K and the heat pipes farther away had a thermal conductivity of 20,000 W/m·K. For the second design, all the heat pipes had a thermal conductivity of 40,000 W/m·K.

3.3 Six-Strut Support System

The mechanical support for the cavity is carried out by the six-strut system that is made to constrain an object's six degrees of freedom and minimize the optical axis offset. We followed some advice found from an article on how to implement the six-strut system to any object [9]. The struts are made orthogonally with one in $z^{¿}$, two in $x^{¿}$, and three in $y^{¿}$ directions, as seen in Figure 5.

The struts were designed in this way to provide the strongest constraint in the direction of most disturbances, which would be in the $y^{\hat{}}$ in this case because of the additional vibrational disturbances from the floor. However, the lengths and positions of the struts can be altered to accommodate environmental restrictions.

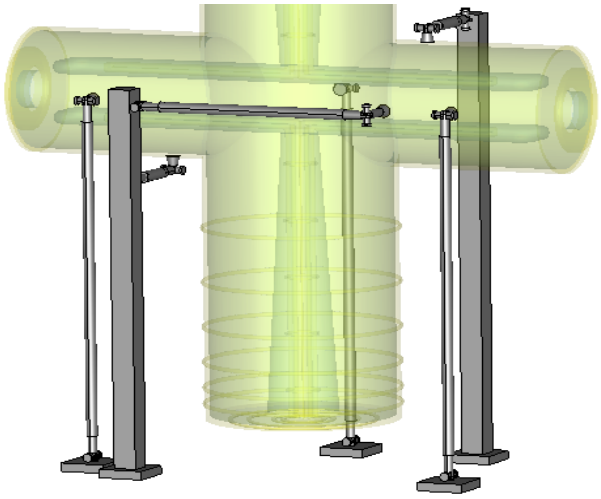

Figure 5. Here is a visual for the six-strut system implemented into the QWR multiphysics design. Here one can see what a strut looks like and how it is actually supposed to support the cavity as well as minimize the optical axis offset.

4. RESULTS

4.1 Thermal Results

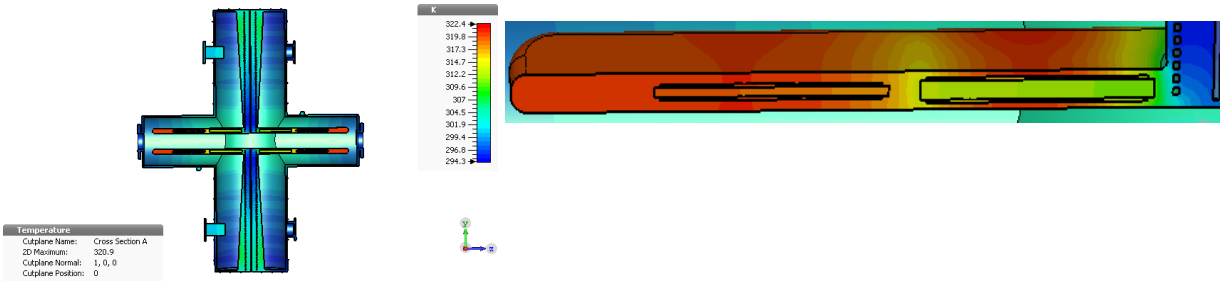

Figure 6. The temperature distribution for the first design of heat pipes. The bottom picture is an image zoomed to the surface of one of the capacitors to show the temperature distribution. The maximum temperature in the stem is 308 K and the maximum temperature in the capacitors is 322 K.

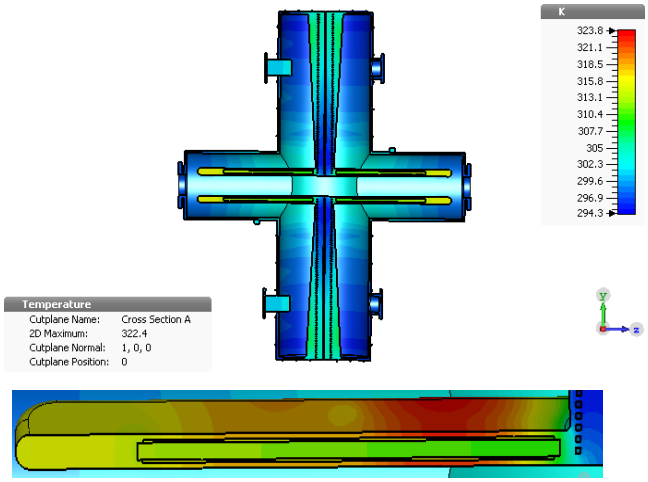

Figure 7. The temperature distribution for the second design of heat pipes. The bottom picture is an image zoomed to the surface of one of the capacitors to show the temperature distribution. The maximum temperature in the stem is 308 K and the maximum temperature in the capacitors is 324 K.

Figure 6 and Figure 7 show the temperature distributions that resulted from implementing cooling channels and heat pipes into the cavity. The temperature distributions are similar to each other and provide a much smaller temperature increase than before.

4.2 Results of Mechanical Analysis

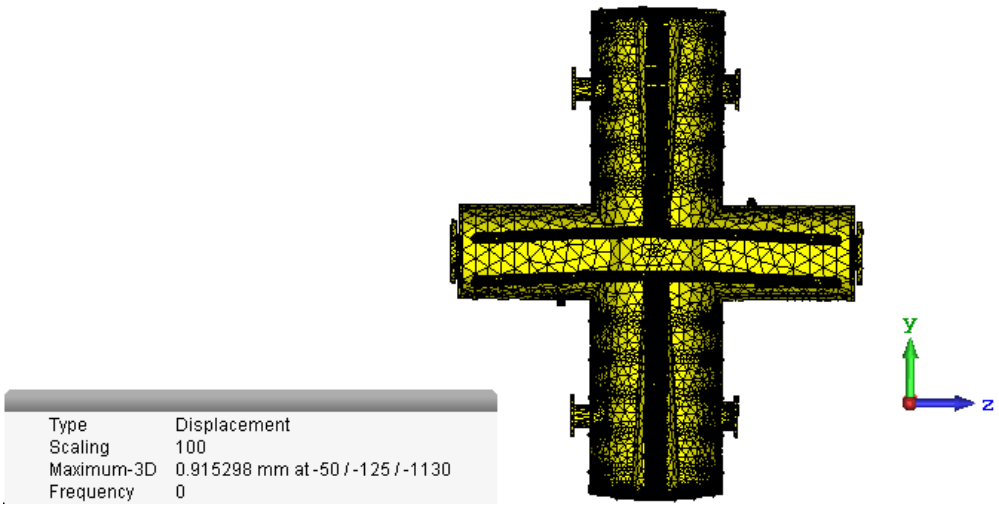

Figure 8. Deformation due to thermal expansion with the first design of heat pipes. These are deformations scaled 100 times. The drop at the capacitor's edges are due to gravity, also magnified 100 times.

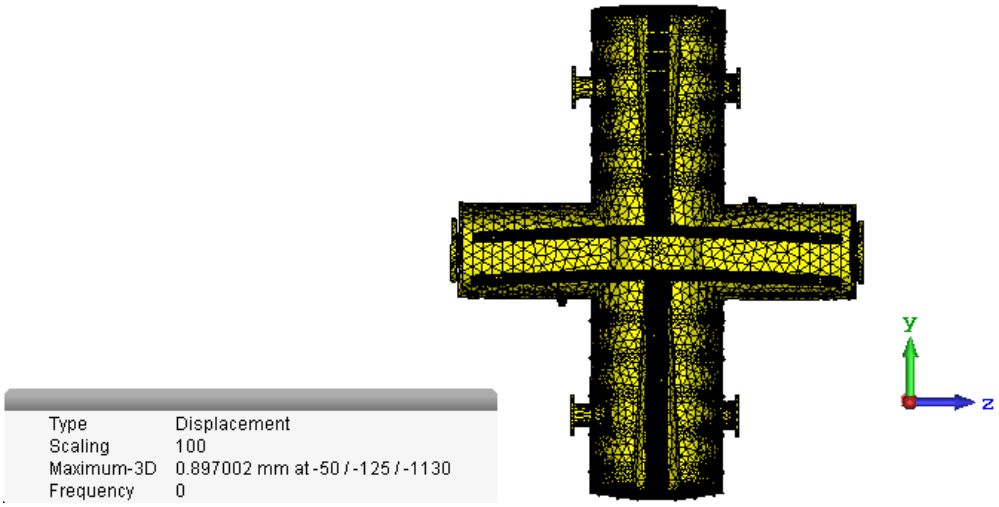

Figure 9. The deformation due to thermal expansion with the second design of heat pipes. These are deformations scaled 100 times. The drop at the capacitor's edges are due to gravity, also magnified 100 times.

Deformations due to thermal expansion with the temperature distributions in Figures 6 and 7 are shown in Figures 8 and 9. These deformations are scaled 100 times, so that they could be visible. The resulting deformations are very similar with slight variations, which results in similar changes in the resonance frequency. The change in the resonance frequency due to the first design is 5 kHz and the second design is 4 kHz. One main goal of the multiphysics design is to minimize the change in the resonance frequency, making it 0 if possible. However, the tuners implemented into the design on the upper and lower left of the cavity are movable to correct changes in resonance frequency up to approximately 20 kHz.

5. CONCLUSION

The final designs of the quarter-wave resonator separator include cooling channels, heat pipes, and a six-strut system. These designs differ by the structure of the heat pipes. However both the designs of the heat pipes result in a small change in the resonance frequency that can be corrected using tuners.

6. ACKNOWLEDEMENTS

I am grateful for the opportunity to conduct research at the Facility for Rare Isotope Beams through Michigan State University's Physics REU Program. I would also like to thank Peter Ostroumov for allowing me to work on this specific project and Alexander Plastun whose direct efforts and guidance allowed me to make such progress in my work.

References

[1] National Superconducting Cyclotron Laboratory, https://www.nscl.msu.edu/users/equipment.html

[2] Pozar, David M. Microwave Engineering. 4th ed. Hoboken, NJ: John Wiley & Sons, 2012.

[3] "Thermal Expansion," HyperPhysics, , accessed August 20, 2018, http://hyperphysics.phy-astr.gsu.edu/hbase/thermo/thexp.html.

[4] "Energy Stored on a Capacitor," HyperPhysics, , accessed August 20, 2018, http://hyperphysics.phy-astr.gsu.edu/hbase/electric/capeng.html.

[5] Boundless. "Boundless Physics." Lumen. Accessed August 20, 2018. https://courses.lumenlearning.com/boundless-physics/chapter/magnetic-fields-and-maxwell-revisited/.

[6] CST Particle Studio, https://www.cst.com/products/cstps

[7] Thermacore, https://www.thermacore.com/frequently-asked-questions/#70

[8] "Wits, IR. Wessel W., Dr. \"Two–Phase Heat Transfer Principles.\" University of Twente. Accessed July 27, 2018. https://home.ctw.utwente.nl/witsww/index.php/research/two–phase–principles."

[9] W. Thur, R. DeMarco, B. Baldock, K. Rex, in Proceedings of the 5th International Workshop on Accelerator Alignment, ANL/FNL Illinois, 1997, eConf C971013, IWAA (1997). http://www.slac.stanford.edu/econf/C971013/papers/045.PDF

STUDENT JOURNAL OF PHYSICS

Fitting IceCube Neutrino Path models using Neural Networks

Mohammed Mohammed Salih [1], Jessie Micallef [2,3], Dirk Colbry [2]

[1] Department of Computer Science and Engineering, Junior, University of Michigan, Ann Arbor, USA
[2] Department of Computational Mathematics, Science and Engineering, Michigan State University, East Lansing, USA
[3] Department of Physics, Michigan State University, East Lansing, USA

ABSTRACT

To check if machine learning is an appropriate method to attack the problem of neutron detection in IceCube experiment, a virtual IceCube simulator (VIceCube) was created which generates phantom data to simplify and control the data set. Machine learning techniques (neural networks) has been tested on the phantom data to determine the limitations of the approach such as sensitivity to noise and measurement precision/error.

Keywords: *Neutrino, IceCube, Machine Learning*

1. INTRODUCTION

Neutrinos are small, fundamental, nearly massless particles. Their rare interaction with matter makes it difficult to determine their precise mass along with many of their other properties. Researchers on the IceCube experiment are working to constrain the values of the neutrino masses, along with searching for sources of astrophysical neutrinos and using them to search for dark matter. The IceCube Neutrino Observatory [1] is a particle detector located inside the ice in the South Pole that records the interactions of neutrinos with ice (Figure 1). The instrumented ice spans about a 1km cubed grid, with the detectors arranged in a hexagonal shape buried about 1.5 km under the ice. Each hole in the grid has a 2.5 km string, with 60 light sensors called photomultiplier tubes spaced out along the last kilometer. The interaction of a neutrino with the ice creates a charged particle that travels faster than the phase velocity of light in ice, making it emit light inside of the ice along its path (Cherenkov radiation). The emitted photons are detected by the photomultiplier tubes. Using the array of detectors' measurements, analytics and machine learning can be used to determine the angle, origin of interaction, speed, and energy of the incoming neutrino.

The focus of my current project is to reconstruct many neutrino interactions to gain statistics to better understand neutrino properties and sources. To check if machine learning is an appropriate method to attack this problem, a virtual IceCube simulator (VIceCube) was created which generates phantom data to simplify and control the data set. Machine learning techniques (neural networks) are tested on the phantom data set to determine the limitations of the approach such as sensitivity to noise and measurement precision/error.

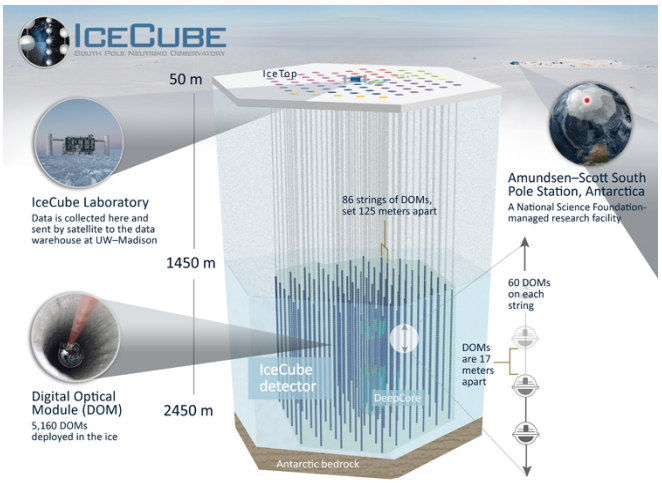

Figure (1): Full IceCube detector with 5160 detectors arranged in a 3D grid. [2]

2. METHODS

Phantom data generation uses random inputs and a model of the neutrino/ice interactions to generate artificial data (forward problem). This artificial data is then used as training data for a machine learning model to see if the inputs can be learned (inverse problem). Since everything is simulated, the true inputs are known and full evaluation of the approach can be conducted. The outputs of the simulator are the origin of interaction of the neutrino, which are x and y coordinates, and the angle as the neutrino crosses into the detector. The origin of interaction and the angle are randomly generated using a uniform distribution. The input generated by the simulator is the charge that each sensor measures as a "virtual" neutrino goes past each sensor. The charge is correlated to how much energy each sensor detects as a neutrino passes through the detector. For this simulator there are 121 "virtual" sensors. The current simulator uses a 2 dimensional grid (Figure 2) which will be upgraded to 3 dimensions in our future work. The neutrino follows a path given the angle that the particle hits the virtual IceCube. Given the origin of interaction of a neutrino, the following method was used to generate a charge for each sensor:

$$Charge = \frac{(MaxDistance - DistanceToEachNode)^2}{MaxDistance^2}.$$

Max Distance is the maximum distance a sensor can be from the path, which is a constant. Distance to each sensor is the distance of each sensor to the origin of interaction of the neutrino. An example of how the simulator works is shown in Figure 3.

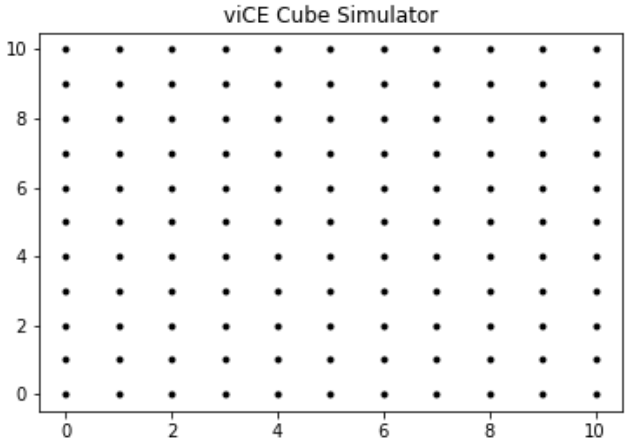

Figure (2): Example of a 2 dimensional grid with each Sensor marked evenly from 0 - 10.

To simplify the problem for machine learning, the initial simulator was tested without the path detection inside of Tensorflow [3]. Tensorflow is an open-source machine learning framework by Google. Given the simple nature of the phantom data, the neural network model was straightforward to train and was able to accurately predict the origin of interaction given only the charges of the sensors. To further test the approach, a Gaussian noise was added to the charges.

Origin_x	Origin_y
5.21925591133953	0.172719507669898

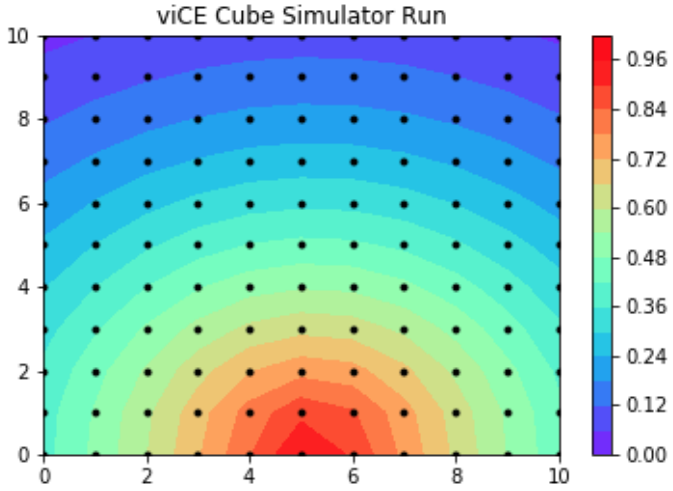

Figure (3): An example of a run of our simulator only with the real origin of interaction detected without a neutrino path

3. RESULTS

Using phantom data created by the VIceCube simulator (Figure 3), the hyper parameters for our neural network were determined. We have used a convolutional neural network (CNN), which consists of an input, output layer and multiple hidden layers. DCross validation was used to split our testing and training data. The Mean Squared Error (MSE), which measures the average difference between the estimated values and the real values, was used to determine the precision of the algorithm. As the initial simulator was rather simple, it had a very low error, close to 0. There was very little difference between the estimated and real values, and therefore the simulator is a good Machine Learning Predictor.

To understand how the machine learning responds to noise in the system, a Gaussian noise was added to the phantom data generator (Figure 4). The noisy data was trained and predicted with multiple intervals of Gaussian Noise (Figure 5), which shows an expected linear reduction in the performance of the predictor, making it more challenging to determine the hyper parameters.

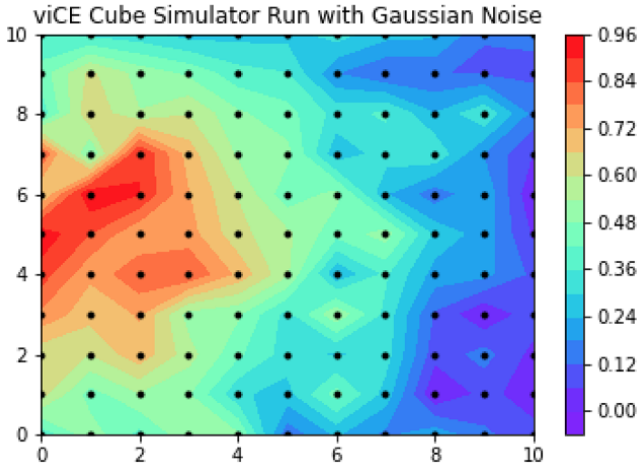

Figure 4: VIceCube simulator with Gaussian Noise. Sigma of noise = 0.1.

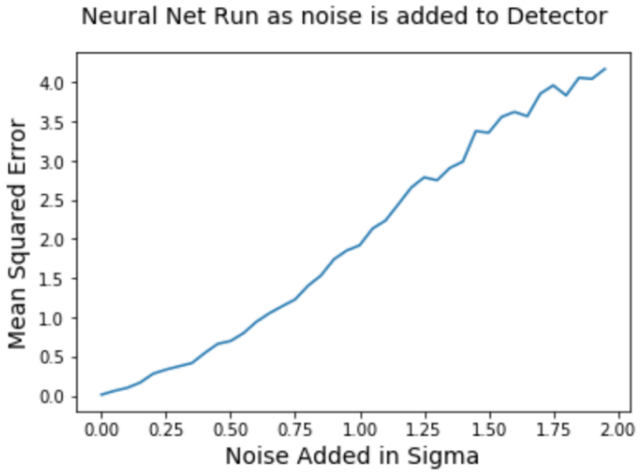

Figure 5: Comparison of Noise Added vs Mean Squared Error

4. FUTURE WORK

To begin this project, we started simple so we could build this study step by step to explore the robustness of using machine learning for a more complex data set. Future work for this project includes using a 3D simulator rather than the 2D simulator. Using 3D would be more accurate; however it would only simulate a cube and not a hexagonal ring. Predicting in 3D would likely be much more difficult, thus our predicting accuracy will be lower than the accuracy of the 2D detector. Other factors that have not been taken into account in this simulator are the energy and time components. We plan to add those in the future. Also, since we did not have access to the IceCube data during this project, we plan to test our neural network approach on the real IceCube data and measure its performance. The ultimate goal of the IceCube project is to determine the mass of the neutrino, and we believe that machine learning can be a useful tool to achieve this goal.

References:

[1]: Goldschmidt, A. (2002). Scientific Goals of the IceCube Neutrino Detector at the South Pole. *Nuclear Physics B - Proceedings Supplements,110*, 516-518. doi:10.1016/s0920-5632(02)01552-9

[2]: Icecube.wisc.edu. (n.d.). *Detector*. [online] Available at https://icecube.wisc.edu/science/icecube/detector

[3]: TensorFlow. (2018). *TensorFlow*. [online] Available at: https://www.tensorflow.org/

Investigating the perturbed geometries of vortex rings in free fall through another liquid

Dripto Biswas[**]

3rd Semester, School of Physical Sciences,
National Institute of Science Education and Research,
Orissa, Jatani - 752050

Abstract. The goal of this paper is to theoretically investigate the origin of the standing wave-like perturbation observed on the vortex rings of a fluid, falling through another liquid. We simplified the Navier-Stokes equation based on observational evidence from related research, and showed that there exists a steady-state velocity field with the required wave-like characteristics. For better visualization we also plotted the velocity field.
Keywords: Vortex rings, Interficial Surface tension, Navier-Stokes Equation, Reynold's Number, Laplace Equation, Lamb-Oseen Vortex, Vorticity.

1. INTRODUCTION:

Vortex rings, also called a toroidal vortex, is a torus-shaped vortex in a fluid; that is, a region where the fluid mostly spins around an imaginary axis line that forms a closed loop. Some liquids are known to form vortex rings when dropped into other liquids having suitable properties [1, 2].The 'drop to vortex ring' formation was first observed and studied by J.J Thomson and H.F Newall [1].They investigated the dependence of the formation of vortex rings from drops, on various factors like interfacial surface tension between the two liquids, the ratio of $\frac{\eta}{d}$ (which is a measure of the Reynolds number for the falling vortex ring) and initial impact speed [1]. Vortex rings are seen to form when drops of ink are released into still water(see Fig. 1). The breakup of the ring into self-similar structures [1] is preceded by a wave-like perturbation which is observed to form throughout the vortex ring at almost the same time.

Keywords: Vortex rings, Interficial Surface tension, Navier-Stokes Equation, Reynold's Number, Laplace Equation, Lamb-Oseen Vortex, Vorticity.

[**] dripto.biswas@niser.ac.in

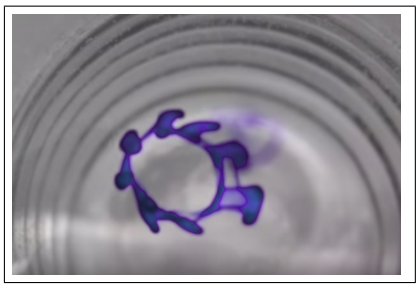

(a)

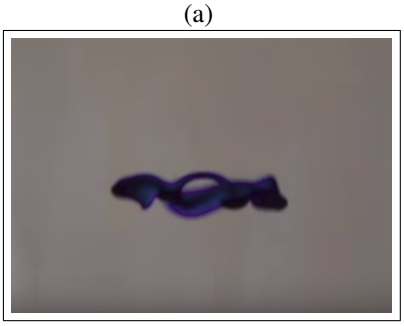

(b)

Fig. 1: (a) shows the top view of the perturbed vortex rings in free fall while (b) shows the side view.

For our purposes, we assume the drop to have been released just below the surface of the water with very low initial velocity. High velocity tends to introduce high circulation in the initial drop, which leads to the breakup of the ring/drop structure(it may diffuse before forming a well-defined toroidal shape) [1–3].

According to the paper by Baumann N. *et al.* [2], low Reynolds number is a characteristic of the flow of the falling vortex ring. We shall use this crucial observation while simplifying the Navier-Stokes Equation.

We assume that the vortex ring has a well-defined toroidal structure (since there is negligible diffusion of the vortex ring [1]) and thereby attempt to mathematically model the velocity field of the vortex ring. We apply the Navier-Stokes equation to the volume enclosed by the toroidal surface. Two dimensional plots of the final velocity field, and a three dimensional plot of the perturbation velocity field is provided. The perturbation velocity field is possibly the reason behind the observed standing wave-like pattern on the ring. In the following section, we simplify and solve the Navier-Stokes equation to get the solution representing the falling vortex ring after reaching steady-state.

2. MATHEMATICAL MODELLING:

Treating the ring as a compact object falling through a viscous liquid, we conclude that it must reach a terminal falling velocity, after steady-state flow has been established. We use a cylindrical coordinate system (ρ, ϕ, z), with the origin of coordinates being the geometric centre of the unperturbed

toroid, co-moving with the falling vortex ring. Let the vortex ring velocity field after terminal velocity has been attained, be given by $\vec{\Psi}(\rho, \phi, z)$ and the direction of motion(downward) be along the z-axis. Note that, we neglect the energy dissipation once steady-state has been attained.

Let $\vec{\epsilon} = \epsilon(\rho, \phi, z)\hat{k}$ denote the velocity perturbation introduced into the vortex ring along the z-axis. The reason behind this directional bias is the acceleration due to gravity vector $\vec{g}$ pointing along the z-axis.

The Navier-Stokes equation is given as [5],

$$\frac{\partial \vec{\Psi}}{\partial t} + (\vec{\Psi} \cdot \nabla)\vec{\Psi} - \nu \nabla^2 \vec{\Psi} = -\nabla w + \vec{g} \tag{1}$$

where $w = \frac{p}{d}$, p being the pressure and d the density of the fluid and ν denotes the kinematic viscosity.

We neglect the $(\vec{\Psi} \cdot \nabla)\vec{\Psi}$ (convective) term as the Reynolds number for the flow was observed to be quite less [2], implying the dominance of viscous forces over inertial forces. Therefore,

$$\frac{\partial \vec{\Psi}}{\partial t} - \nu \nabla^2 \vec{\Psi} = -\nabla w + \vec{g} \tag{2}$$

We consider ν to be a constant, as all related parameters(like temperature, density of liquid etc.) are constant. Let $\vec{\Phi} = \vec{\Psi} + \vec{\epsilon}$ denote the perturbed velocity field. Since $\vec{\Phi}$ also must satisfy the Stokes equation, we have,

$$\frac{\partial \vec{\Phi}}{\partial t} - \nu \nabla^2 \vec{\Phi} = -\nabla(w + w') + \vec{g}$$

or,

$$\frac{\partial \vec{\Psi}}{\partial t} - \nu \nabla^2 \vec{\Psi} + \frac{\partial \vec{\epsilon}}{\partial t} - \nu \nabla^2 \vec{\epsilon} = -\nabla w - \nabla w' + \vec{g}. \tag{3}$$

Using eqn. 2 for $\vec{\Psi}$ and eqn. 3, we now have,

$$\frac{\partial \vec{\epsilon}}{\partial t} - \nu \nabla^2 \vec{\epsilon} = -\nabla w'. \tag{4}$$

As discussed above, the vortex ring is assumed to have attained a terminal falling velocity. We are looking for stationery state solutions to the Navier-Stokes equation, since any system under the influence of balanced external forces tend to evolve into stationery states. In other words,

$$\frac{\partial \vec{\Phi}}{\partial t} = \frac{\partial \vec{\Psi}}{\partial t} + \frac{\partial \vec{\epsilon}}{\partial t} = 0. \tag{5}$$

But, with respect to the co-moving origin, the original flow field $\vec{\Psi}$ is time-independent once terminal velocity is achieved(since the energy dissipation is neglected after the ring reaches terminal velocity) This implies that,

$$\frac{\partial \vec{\Psi}}{\partial t} = 0 \tag{6}$$

Thus, from eqn. 5 , we observe that $\vec{\epsilon}(\rho, \phi, z)$ is a stationary time-independent perturbation. It follows that

$$\frac{\partial \vec{\epsilon}}{\partial t} = 0. \tag{7}$$

Also, if $\nabla w' \neq 0$, there exists a net external force, which in turn will make the velocity field non-stationary(time-dependant). Therefore, $\nabla w' = 0$. Eqn. 4 then simplifies to,

$$\nabla^2 \vec{\epsilon} = 0. \tag{8}$$

Now, we observe that $\epsilon(\rho, \phi, z)\hat{k}$, has no radial or angular component but only a component along the z-axis. The vector Laplacian in cylindrical coordinates is given by [4],

$$\nabla^2 \vec{A} = (\nabla^2 A_\rho - \frac{A_\rho}{\rho^2} - \frac{2}{\rho^2}\frac{\partial A_\phi}{\partial \phi})\hat{r} + (\nabla^2 A_\phi - \frac{A_\phi}{\rho^2} + \frac{2}{\rho^2}\frac{\partial A_\phi}{\partial \phi})\hat{\phi} + \nabla^2 A_z \hat{k}$$

Substituting $\vec{\epsilon}$ for $\vec{A}$ above, and noting that $\epsilon_\rho = \epsilon_\phi = 0$, we further simplify eqn. 8 as,

$$\nabla^2 \vec{\epsilon} = \nabla^2 \epsilon \hat{k} = 0. \tag{9}$$

This is the Laplace equation, whose solutions are known as harmonic functions. Given appropriate boundary conditions, we can find the exact three dimensional harmonic solutions on a toroid.

We proceed to look for suitable solutions of the Laplace equation on a toroid of inner radius a and outer radius b, having boundary velocity profiles which are 2π periodic in nature. The most general solution to the Laplace equation can be found by assuming the separability of components in the solution as [4],

$$\epsilon(\rho, \phi, z) = R(\rho)G(\phi)Z(z). \tag{10}$$

Solving the equation and separating the components we get,

$$Z(z) = A_z e^{kz} + B_z e^{-kz} \tag{11}$$

$$G(\phi) = A_\phi \cos(n\phi) + B_\phi \sin(n\phi) \tag{12}$$

where n is a positive integral constant and k is a real number.

Now, we note an important feature of $\epsilon(\rho, \phi, z)$, due to the continuity equation. Since, $\nabla \cdot \vec{\Phi} = 0$ and $\nabla \cdot \vec{\Psi} = 0$ (the flow being incompressible), we must have $\nabla \cdot \vec{\epsilon} = 0$. This leads to the equation,

$$\frac{\partial \epsilon}{\partial z} = 0$$

However, from eqn. 10 we see that this implies $k = 0$ in the expression for $Z(z)$. In other words, the perturbation $\vec{\epsilon} = \epsilon(\rho, \phi)\hat{k}$ is independent of z. The remaining differential equation for the $R(\rho)$ term is given by,

$$\frac{\rho^2}{R}\frac{d^2 R}{d\rho^2} + \frac{\rho}{R}\frac{dR}{d\rho} = n^2 \tag{13}$$

whose general solution is,

$$R(\rho) = A_\rho \cosh(n \log \rho) + iB_\rho \sinh(n \log \rho) \tag{14}$$

where $i = \sqrt{-1}$. We consider only the real part, and write the final solution as,

$$\epsilon = C(a, b) \cosh(n \log \rho) \sin(n\phi) \tag{15}$$

where $C(a, b)$ is a combination of the constants, and it depends on at least 2 initial conditions, most possibly the inner and outer radius a and b. n denotes the number of nodes observed on the vortex ring, which we suspect depends on the total energy of the system. Obviously, this is not the general solution, but we shall use this form for further plots.

3. RESULTS:

The boundary conditions can theoretically be determined by careful observation using precise instruments, and is currently beyond the scope of this paper. We have simply chosen a set of values for the constants(based on trial and error) and have constructed a plot of the solution on a toroid of inner radius $a = 0.5\ cm$ and outer radius $b = 0.6\ cm$ The following are the three dimensional volume plots of the magnitude of the perturbation velocity field $\vec{\epsilon}$. It is understood that this field is superposed along the $\hat{k}$ direction on $\vec{\Psi}$. The positive and negative values at various points of the plot correspond to the velocity magnitudes at those points, having directions $\hat{k}$ and $-\hat{k}$ respectively.

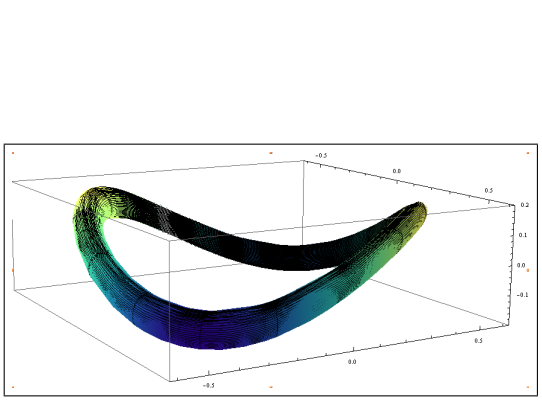

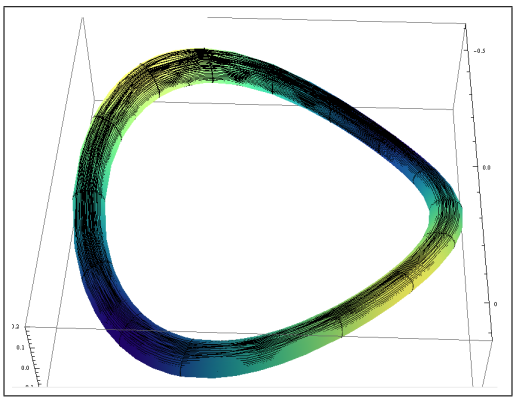

Fig. 2 (Left) and Fig. 3 (Right): 3-D plot of $\vec{\epsilon} = \epsilon\hat{k}$(2 nodes)

Yellow - positive values ; Blue - negative values

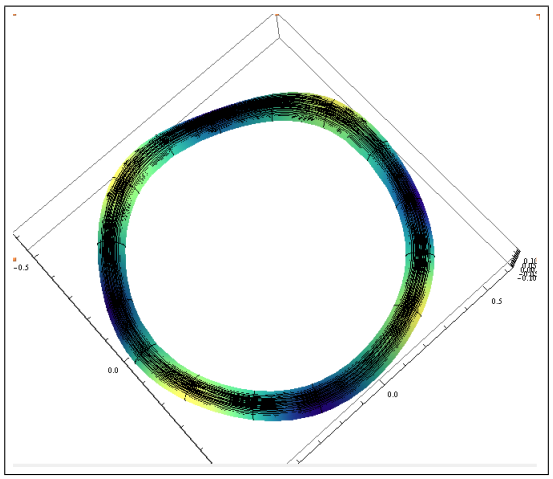

Fig. 4: 3-D plot of $\vec{\epsilon} = \epsilon\hat{k}$(4 nodes)

Yellow - positive values; Blue - negative values

It is not difficult to imagine that the shape of the toroidal ring will be the same (almost) as the one depicted here, as every point inside the toroid develops a new velocity component along z-axis, consequently pushing it upwards or downwards depending on ϕ.

To give an idea of the perturbed velocity field $\vec{\Phi}$, we consider the circulation field to be represented by a Lamb-Oseen vortex having constant total circulation Γ and a core vortex radius of 0.01 cm. Our origin for the subsequent plots, is the centre of the circular cross-section of the toroid, and the two dimensional graphs represent the corresponding cross-section plane of the toroid. We assume that after attaining terminal velocity, the dissipation of energy of the system being negligible, the core radius is preserved. The two dimensional velocity field is then given by,

$$\vec{V}(r,\theta) = \frac{\Gamma}{2\pi r}(1 - e^{\frac{-r^2}{r_c^2}})\hat{\theta} \tag{16}$$

where $r_c = 0.01cm$ denotes the core radius. Note that this r is different from the ρ in the equations derived above. For the plot, $\rho = 0.55 + r\cos\theta$ from simple geometry. Thus, the perturbation field $\vec{\epsilon}(\rho, \phi, z)$ can be written in terms of (r, θ) for given values of ϕ. We chose to plot the total velocity field at a node ($\phi = \frac{\pi}{4}$) and an anti-node($\phi = \frac{3\pi}{4}$) for a 2-node vortex ring. The plots are shown below.

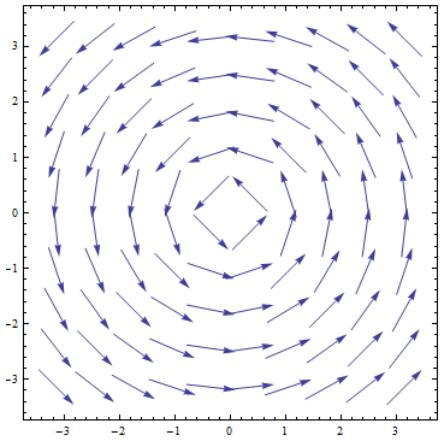

Fig. 5: Unperturbed velocity field of a Lamb-Oseen vortex

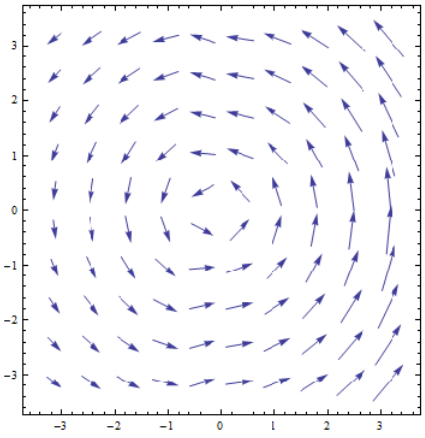

Fig. 6: Perturbed velocity field at $\phi = \frac{\pi}{4}$

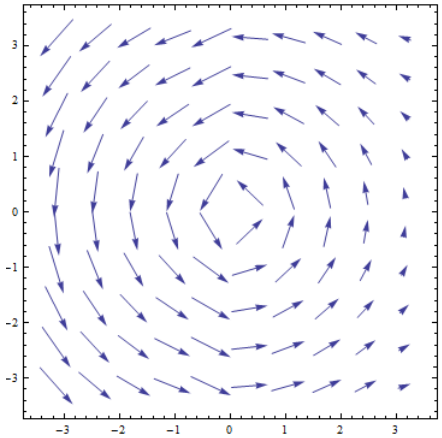

Fig. 7: Perturbed velocity field at $\phi = \frac{3\pi}{4}$

Fig. 5 shows the velocity field in the cross-section of the unperturbed vortex ring(modelled after a Lamb-Oseen Vortex). Thus, the arrows denote the direction of the field at a particular point on the cross-section, while their lengths denote the magnitude of the flow velocity at that point. Fig. 6 and Fig. 7 denote the velocity profile of the cross-section of the perturbed vortex ring at a node and anti-node respectively. Note how, in Fig. 6 and Fig. 7, the velocity field on one side is smaller than the other side. This is due to every point being forced upwards/downwards on superposition of $\vec{\epsilon}$ to $\vec{\Psi}$. In Fig. 6, the center of mass of the system(the origin in this case) develops a net upward velocity, as there is greater momentum in the upward direction compared to the downward direction. Similarly, in Fig. 7, the center of mass develops a net downward motion due to greater momentum in the downward direction.

4. CONCLUSION:

We developed a theoretical model of the perturbed vortex ring, in an attempt to justify the symmetric wave-like patterns observed on it. The angular component, is clearly responsible for the standing wave-like nature of the perturbation.

Experiments may be performed to show that these rings indeed reach a terminal velocity before the observed perturbations set in. For our approximate model to be correct, it is essential for the system to reach a steady-state while falling through the liquid.

We conclude with one last remark on what might happen after the perturbation sets in. This should primarily depend on the total circulation Γ of the vortex ring. Note that the perturbation field $\vec{\epsilon}$ has a vorticity given by $\omega = \nabla \times \vec{\epsilon}$. Also, the total circulation due to ω can be calculated as $\Gamma_\epsilon = \int\int_S \omega \cdot ds$, where the integral is over the bounding surface of the toroid. Now, if $\frac{\Gamma_\epsilon}{\Gamma} << 1$, the perturbation creates a standing wave-like pattern with low amplitude, but should not disintegrate the ring, as the circulation still remains strong enough to maintain a compact structure. In the two dimensional plots shown above, this will lead to all the 3 plots looking similar to each other with slight differences. However, if $\frac{\Gamma_\epsilon}{\Gamma}$ is close to 1, soon after the perturbation sets in, the ring should disintegrate, possibly into new drops(branching off from the anti-nodes). In the two dimensional plots, we would observe one side of the circular cross-section of the ring to move much faster compared to the other side, thereby de-stabilising the circulation of the vortex ring. Even this claim may be verified with further experiments which can study the relation between unstable or stable vortex rings and the ratio $\frac{\Gamma_\epsilon}{\Gamma}$. Qualitatively, the circulation due to $\vec{\epsilon}$ should be much smaller than the circulation due to the unperturbed velocity field of the vortex ring, in order to maintain a well-defined toroidal shape.

5. ACKNOWLEDGEMENT:

I would like to thank Professor Victor Roy of the School of Physical Sciences, NISER , without whose guidance, this theoretical investigation would not have been possible. I would also like to

thank the academic administration of NISER for providing me the opportunity to undertake this interesting project.

References

[1] Thomson J.J, Newall H.F. 1885. On the formation of vortex rings by drops falling into liquids, and some allied phenomena. Proc. R. Soc. Lond. 1886 39, 417-436.

[2] Baumann N,Joseph DD,Mohr P,Renardy Y.1992. Vortex rings of one fluid in another in free fall.

[3] Chapman D.S. and Critchlow P.R. 1967.Formation of vortex rings from falling drops. J. Fluid Mech. 29, 177.

[4] Dobek S.2012.Fluid dynamics and the Navier-Stokes Equation.

[5] Prof Dr. I. Nasser, Phys 571,T-131,22-Oct-13

Nuclear Radiation Measurement using Thermoluminescence Technique

Shashank Kumar[1], Pradeep Narayan[2], Sumita Srivastava[3]
M.Sc. Physics III[rd] Semester
[1,3] Department of physics, Pt. L.M.S. Government PG College, Rishikesh (Autonomous College)

[2] Defence Laboratory, DRDO, Jodhpur

Abstract: In this study, the standard Thermoluminescence dosimetric (TLD) material ($CaSO_4$:Dy) in the form of Teflon discs have been studied for their thermoluminescence property. The TL sensitivity of the $CaSO_4$:Dy Teflon discs has been investigated while irradiating them with gamma radiation emitted from ^{60}Co radioactive source. The discs were calibrated with different radiation exposure and the unknown radiation exposure was estimated using this method. Known $CaSO_4$;Dy discs were collected from the Defence Laboratory DRDO, Jodhpur in the form of Teflon discs which were annealed by putting them in an oven for 4 to 6 hours at 300 ^{0}C. The TL integral count and TL glow curve of the discs were recorded by a TLD Reader. On the basis of the obtained data from our observations using TLD Reader the TL sensitivity of $CaSO_4$:Dy in units of AU/R/mg (Arbitrary unit per Roentgen per milligram) were estimated, where 1 Roentgen is the quantity of X-radiation or gamma radiation that produces an electrical charge of 2.58×10^{-4} Coulomb in a kg of air at standard temperature and pressure (STP). Future prospects of the $CaSO_4$:Dy Teflon discs are discussed.

Keywords: Thermoluminescence, $CaSO_4$:Dy Teflon discs, Radiation, Exposure, Glow curve

1. INTRODUCTION

Thermoluminescence (TL) is a form of luminescence that is exhibited by an insulator or a semiconductor which is observed when the solid is thermally stimulated. TL is thermally stimulated emission of light following the absorption of energy from radiation [1]. The TL characteristics of a material are expressed by a few parameter such as order of kinetics, activation energy and frequency factor. The knowledge of these parameters is essential for the understanding of TL process occurring in a phosphor. There are many experimental techniques developed on the basis of glow curve shape, heating rate, phosphorescence decay etc. [2]. During the TL process, part of energy absorbed by the material is re-emitted during heating in form of light. The plot of the TL intensity (light output) as a function of rising temperature exhibits one or more peaks is called a glow curve. The glow curve provides a useful tool for studying the traps and trapping parameter (such as trap depth E, kinetic order b, frequency factor etc.).[3].

Calcium Sulphate singly doped with dysprosium is an important TLD material which is commercially available as TLD-600. CaSO4:Dy TL material is known to have a very high sensitivity to gamma radiation. Their main dosimetric glow peak is at 220 ^{0}C, with two unstable low temperature peaks at 80 and 120 ^{0}C. At absorbed dose levels above the limit of linearity (i.e.30 Gy for Dy doped TL material, where Gy stands for Gray and 1 Gray is equal to 100 rads and 1 rad is equal to the deposition of 100 ergs of energy per gram of a tissue (100 erg/gm)) a higher temperature peak appears at approximately 250 ^{0}C.

This peak dominates up to the saturation absorbed dose of 1000 Gy for Dy. The spectral emission peak of the Dy-activated TL material is at 478 and 571 nm. At normal ambient temperature the dark fading of the 220 ^{0}C glow peak of the Dy activated TL material is low. Dark fading is the unintentional release of an electron before readout. The glow curve of $CaSO_4$:Dy is shown in Fig. 1.

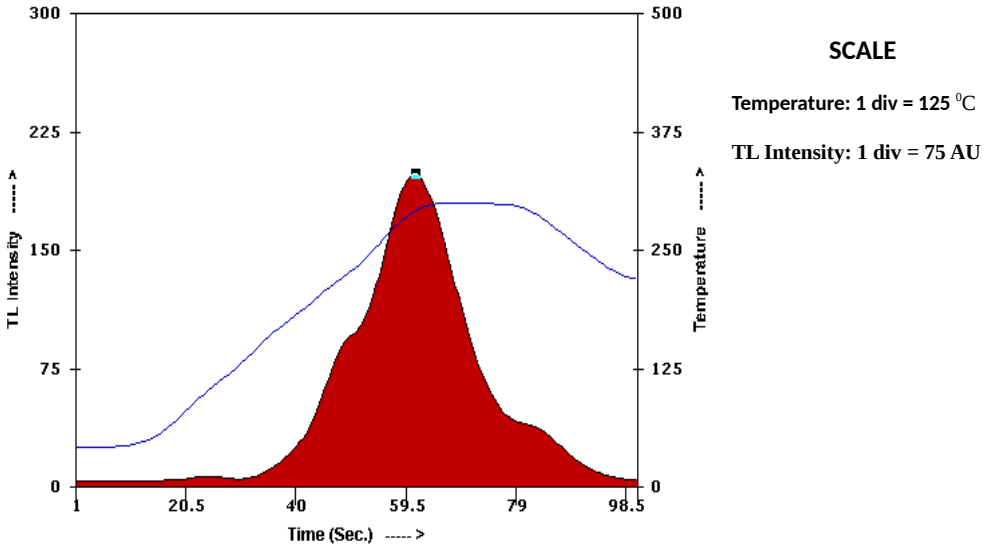

Fig. 1: Graph showing the glow curve of $CaSO_4$:Dy

2. MATERIALS AND METHODS:

Fifty (50) standard TL discs were acquired from old stock of TLD unit of Defence Laboratory, Jodhpur, and have been utilized in this study.

2.1: Sample preparation (annealing):

To ensure complete readout of stored data the TL discs were annealed before taking radiation measurements. All 50 TL discs, were annealed in automatic oven at 270 ^{0}C for four hours and allowed to cool to normal temperature to ensure that the TL discs are free from pre-irradiation.

2.2: TL measurement setup:

A PC controlled TLD Reader (Model: TL1009I, Make: M/S Nucleonix System Pvt. Ltd., Hyderabad, India) was used for investigating the TL property of the material under study. The system has two essential parts; (a) The integral TLD reader and, (b) Personnel computer system with TL data acquisition and analysis software. Entire electronic hardware of the integral TL reader consists of low voltage (LV) and high voltage (HV) supplies, temperature controller and thermocouple amplifier circuits, microcontroller based data acquisition circuits, photomultiplier tube (PMT), heater transformer, PMT current to frequency (I to F) converter and kanthal strip for sample loading with drawer assembly, all are kept in a single enclosure. The TL light output from the sample is detected by the PMT, which is amplified and recorded. The PMT is powered with HV. The recorder continuously records the measured luminescence against time scale or temperature scale or both. Here heating is done by resistive heating method, in which electric current is passed through a planchet so as to raise the sample temperature in a controlled manner.

2.2: Experimental procedure:

2.2.1: Sample exposure with gamma radiation:

The prepared samples (annealed discs) were irradiated in calibrated gamma radiation field of average energy (1.25 MeV) emitted from ^{60}Co sources of Industrial Gamma Radiation Exposure Device (IGRED), Model: Techops-741 at Defence Laboratory, Jodhpur. The radiation from ^{60} ₂₇ is nearly mono-energetic, being made up of two photon energies, 1.17 MeV and 1.33 MeV, giving an average of 1.25 MeV (Technical report, 1987). Here gamma radiation has been used for irradiating the sample. The desired exposure rate and accordingly the irradiation time for the samples were calculated using the standard and calibrated radiation field data provided by Bhabha Atomic Research Centre (BARC), Mumbai. Standard Radiation Field data:

Standard Radiation Field data:

- Source: ^{60}Co, $T_{1/2}$ = 5.27 years (1924 days)
- Exposure rate at 53.3 cm from the source: 118.949 R/h as on 25/07/2012

Calculation of exposure data for sample irradiation:

- Date of experiment: 08/06/2018
- Total time elapsed since calibration: 08/06/2018 – 25/07/2012
  = (06 years) = 2173 days
- Exposure rate $X(t) = X(o).\exp-[(0.693x\ t)/T_{1/2})]$
  $X(t) = 118.949 \times \exp-[(0.693x2173)/1924] = 55.34$ R/h as on08/06/2018
- Exposure rate at 50 cm from the source = $55.34 \times (53.3/50)^2 = 61.80$ R/h

Table 1: Sample Exposure time for different exposure

Sample Exposure time	**Exposure (R)**
30 sec	0.51
1 min	1.03
5 min	5.15
10 min	10.3
50 min	51.5

Five TL Discs for each exposure were packed in an opaque paper and immobilized at 50 cm from the source of the radiation calibration unit and exposed as per calculated exposure time given in Table 1.

2.2.2: Thermoluminescence Measurement:

Teflon discs of $CaSO_4$:Dy was properly kept on the heating element of the TL Reader. After inserting the heating unit at measurement position, the TL measurement sequence was run, glow curve obtained and the TL output data stored in an appropriate file of the computer system of the unit. The integral count within the glow curve was recorded for each TL disc. This procedure was repeated for all five discs of background measurement and the discs for each set of exposure.

2.2.3: Observations:

The TL Integral counts of the $CaSO_4$:Dy Disc for background and exposure are shown in Table 2.

Table 2: TL measured data of $CaSO_4$:Dy

TL Measured Data of $CaSO_4$:Dy Disc (Standard TL Dosimeter)							
Sr. No.	Background TL Counts (A)	Exposure (Roentgen) -R	TL Output (Integral Counts)-AU			Average TL Integral Counts (AU)-(B)	Net TL Integral Counts (B-A)
			Reading-1	Reading-2	Reading-3		
1	877	0.51	1458	1733	1775	1655	778
2	877	1.03	2442	2446	2592	2493	1616
3	877	5.15	10740	9923	12464	11042	10165
4	877	10.3	23283	22600	22014	22632	21755
5	877	51.5	109108	107077	80532	98906	98029
6	877	Unknown (U1)	4181	4362	4624	4389	1788
7	877	Unknown (U2)	27916	25539	23607	25687	12628

The TL emission of CaSo4:Dy disc at different radiation exposure plotted using analysis software of the TLD reader unit and shown in Fig. 2.

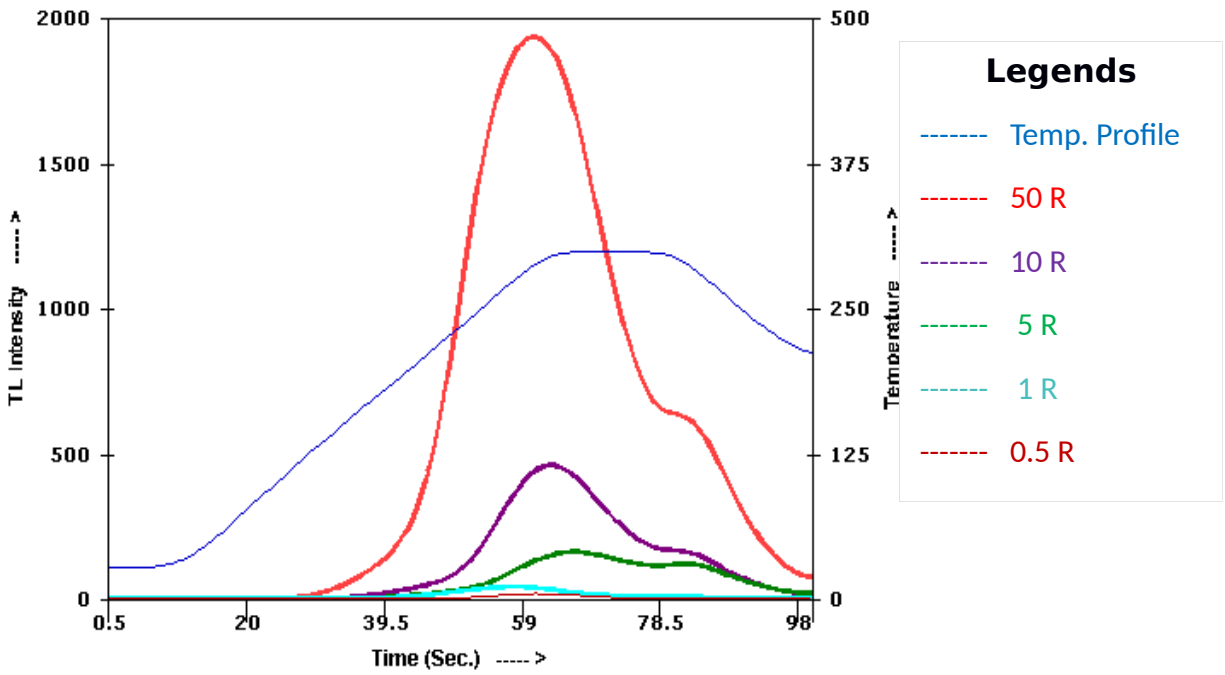

Fig. 2: Graph showing irradiated experimental glow curve of $CaSO_4$:Dy

3. RESULT AND DISCUSSIONS:

3.1: Calibration and TL Sensitivity:

A graph between radiation exposure and net TL integral counts is plotted in Fig. 3. The TL output is found to be directly proportional to the amount of radiation with which the TLD Discs are exposed. TL response of $CaSO_4$:Dy is found to be linear within the studied exposure range 0.5 to 50 R. A linear fitted equation is shown on the graph itself. For the TLD reader used in this study, the TL sensitivity of $CaSO_4$: Dy disc is found to be 1907 Arbitrary Unit (AU)/R.

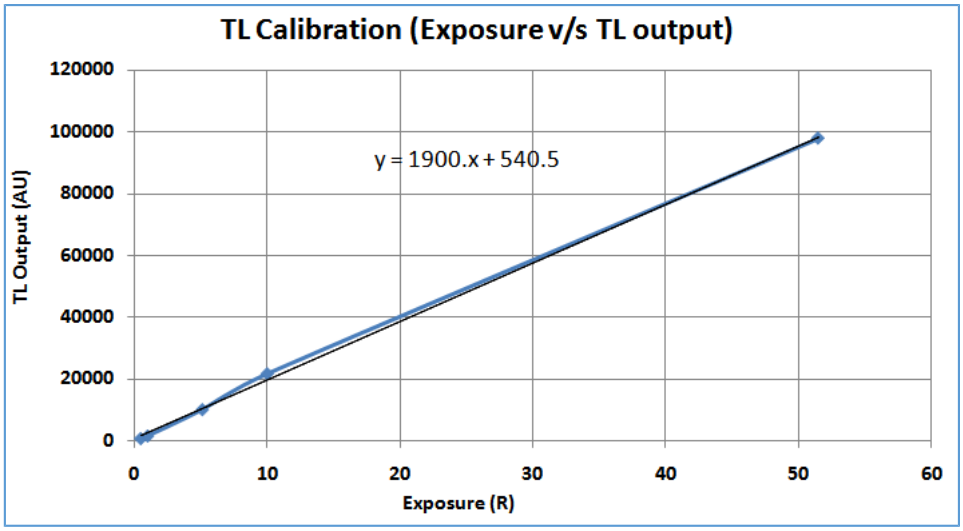

Fig. 3: Calibration Graph (Exposure v/s TL Output)

3.2: Calibration Factor:

From the above graph, the calibration factor of the TL disc as inverse of the slope of the straight line is estimated to be 0.5243 mR/AU. This calibration factor can be used for estimating the unknown exposure received by the TLD disc.

3.3: Measurement of Unknown Dose:

Two sets of $CaSO_4$:Dy discs (five discs in each set) were exposed with unknown gamma doses and their TL was measured under the identical setup of the TLD reader used during the calibration. The exposure measured by this TL technique vis-a-vis the unknown test exposure is given in Table 3. The percentage error in unknown dose estimation using CaSo4:Dy TL material is found to be within 10%, which is acceptable for radiation protection dose estimation.

Table 3: Unknown dose estimation using $CaSO_4$:Dy Disc

Sample ID	TL output (AU)-A	Calibration Factor (mR/AU)-B	Estimated Unknown Exposure (mR) = A X B	Declared Exposure (mR)	% Error
U1	3512	0.5243	1841	1648	-10.48%
U2	24810	0.5243	13008	12446	-4.32%

4. CONCLUSIONS:

The TL property of $CaSO_4$:Dy disc has been studied for nuclear radiation measurement. It has linear TL response in the exposure range required for public as well as personnel radiation dosimetry below 50R. Thermoluminescence is a passive radiation detector, which stores the radiation information for longer period and can be read whenever required. Radiation dosimetry using CaSo4:Dy has been established as routine passive dosimetry system for occupational radiation worker and for environmental monitoring.

5. FUTURE PROSPECTS:

Though radiation dosimetry using $CaSO_4$:Dy TL material has been established, the radiation dose measurement at R level is still a challenge. TL study on novel materials can be explored for low level radiation measurement.

6. ACKNOWLEDGEMENT:

Shashank Kumar is thankful to Defence Laboratory, DRDO, Jodhpur for support to carry this work. He expresses his gratitude to supervisor Dr.Pradeep Narayan (Scientist E) Defence Laboratory, Jodhpur and co-supervisor Dr.(Mrs.) Sumita Srivastava of Pt. L.M.S. Government Post Graduate College, Rishikesh for their support and suggestions during preparation of manuscript.

References

[1] A F Mckinlay, *Thermoluminescence Dosimetry;* 1986, ISBN 0-85274-520-6.

[2] Dr. Vij and N. Singh, *Luminescence and related properties of II-VI semiconductors*; Classes of Luminescence; ISBN 1-56072-433-1.

[3] Dr. Hitesh Mandavia, *Thermoluminescence study of ceramic tiles materials*; ISBN 978-93-84044-78-7, 2015.

STUDENT JOURNAL OF PHYSICS

Study of Thermoluminescence Property of Himalayan Stones for Nuclear Radiation Measurement

Manish Joshi[1], Pradeep Narayan[2], Sumita Srivastava[3]

Physics M.Sc. 2nd year/IIIrd Semester

[1,3] Department of physics, Pt. L.M.S. Government P.G. College, Rishikesh (Autonomous College)

[2] Defence Laboratory, DRDO, Jodhpur

Abstract: In this work, the Thermoluminescence (TL) property of Himalayan stones (natural stone) was investigated for their likely applications in nuclear radiation measurement. Twenty six (26) natural stones sample of size varying from 50-100 gm and different colours were selected from the bank of river Ganga at Rishikesh, in a clean carry bag. Powder samples of size 150-212μm were prepared from each stone samples. The prepared powder samples (each weighing 50 mg) were divided into two parts, one part kept for background measurement and the samples from the other part were positioned at 20 cm from the ^{60}Co radiation and irradiated for calculated exposure time 47 min for 300R exposures. The TL integral count and TL glow curve of the samples were recorded by Nucleonix TLD Reader. On the basis of given information by TLD Reader the TL sensitivity of Himalayan stones was discussed in terms of AU/R/mg and Natural Radiation exposure in Himalayan stones was estimated. The future prospects of higher sensitive stones is also discussed.

Keywords: Thermoluminescence, Himalayan stones, Nucleonix TLD Reader, Glow curve, Natural radiation exposure.

1. INTRODUCTION:

Thermoluminescence (TL) is a form of luminescence, exhibited by certain materials, such as some mineral, when some of the previously absorbed energy from electromagnetic or other ionizing radiation is re-emitted as light upon heating of the material. TL characteristics of a material (phosphers) are expressed by a few parameters, such as order of kinetics, activation energy and frequency factors. The knowledge of these parameters is essential for the understanding of TL process occurring in a phosphor. There are many experimental techniques, developed on the basis of glow curve shape, heating rate phosphorescence decay etc [1]. In the TL process, part of energy absorbed by the material is re-emitted during heating, in form of light. The plot of the TL intensity (light output) as a function of rising temperature exhibiting one or more peaks is called a glow curve. The glow curve provides a useful tool for studying the traps and trapping parameter, such as trap depth E, kinetic order b and frequency factor, etc. [2].

2. MATERIALS AND METHODS:

Twenty six (26) natural stone samples were collected from the bank of river Ganga at Rishikesh. Stones sample of size varying from 50-100 gm and of different colours were selected from the river bank in a clean carry bag. After that the sample stones were labeled and then crushed to make fine powder of size varying between 150-212 μm with the help of metal grinder and combination of two sieves respectively. 50 mg of each powder samples were weighed with digital balance and were separated into two sets. One set was kept for background measurement and the other was used for exposure measurement.

manishjoshi781997@gmail.com

2.1.TL measurement setup:

The PC controlled TLD reader (Model: TL10091, make: M/S Nucleonix System Pvt. Ltd., Hyderabad, India) was used for investigation of TL property of the material under study. This system is comprised of two essential parts (1) the integral TLD reader, (2) Personnel computer system with TL data acquisition and analysis software. The integral TLD reader consists of low voltage and high voltage supplies, temperature controller, thermocouple amplifier circuits, microcontroller based data acquisition circuits, photomultiplier Tube (PMT), heat transformer, PMT current to frequency converter and kanthal strip for sample loading with drawer assembly. All these equipments are kept inside a single enclosure. The TL light output from the sample is detected by the photomultiplier tube (PMT), which is amplified and recorded. Here heating is done by resistive heating method, in which electric current is passed through a planchet so as to raise the sample temperature in a controlled manner.

2.2. Experimental Procedures:

The heating profile of the equipment is adjusted as per measurement requirements. In this study, linear heating profile at the rate of 5^0C/Sec was used with constant heating at temperature 300 ^{0}C for 20 sec and another 20 sec allowed for cooling. The prepared powder samples were irradiated in calibrated gamma radiation field of average energy (1.25 MeV) emitted from ^{60}Co sources of Industrial Gamma Radiation Exposure Device (IGRED), Model: Techops-741 at Defence Laboratory, Jodhpur. The γ radiation from $^{60}Co_{27}$ is nearly mono-energetic, being made up of two photon energies, 1.17 MeV and 1.33 MeV, giving an average of 1.25 MeV (Technical report, 1987). The desired exposure rate and accordingly the irradiation time for the samples were calculated using the standard and calibrated radiation field data provided by Bhabha Atomic Research Centre (BARC), Mumbai.

Standard Radiation Field data:

- Source: ^{60}Co, $T_{1/2}$ = 5.27 years
- Exposure rate at 33.3 cm from the source: 303.125 R/h as on 25/07/2012

Calculation of exposure data for sample irradiation:

- Date of experiment: 26/06/2018
- Total time elapsed since calibration: 26/06/2018 – 25/07/2012 (06 years)
- Exposure rate $X(t) = X(o).\exp-[(0.693x\ t)/T_{1/2})]$
  $X(t) = 303.125 \times \exp-[(0.693x6)/5.27] = 137.71$ R/h as on 26/06/2018
- Let us apply inverse square law for calculating exposure rate at 20 cm distance from the source.
- Exposure rate at 20 cm from the source: 137.71 (33.3/20)2 = 381.76 R/h
- Irradiation time for 300 R = 300 / 381.76 h = 0.77 h = 47 min

The prepared samples were divided into two parts, one part kept for background measurement and the samples from the other part were positioned at 20 cm from the ^{60}Co radiation source and irradiated for calculated exposure time 47 min for 300 R exposures.

2.3. Thermoluminescence Measurement:

50 mg of each powder samples were weighed with digital balance, properly immobilized and uniformly spread over the heating element of the TL Reader. The TL measurement sequence was run and the TL output was stored in proper file of the computer system of the unit. This procedure was repeated five times for all the samples (background and exposed).

2.4. Observations:

First we do a run without giving any exposure to the stone samples to determine background (Natural) TL count (AU). Next, we do a run with exposed stone samples to determine TL integral counts (300R) like reading1, reading2….etc. Then we take an average of those TL integral counts (300R). To obtaining net TL integral counts for 300R we subtracted background (Natural) TL counts from average TL integral counts.

We define sensitivity as,

$$Sensitivity = \frac{Net\ TL\ integral\ count}{300\,R}$$

Here unit of sensitivity is AU/R/50mg, where AU is arbitrary unit.

We define,

$$Natural\ radiation\ exposure\left(Roentgen\right) = \frac{Background\left(Natural\right)TL\ count}{sensitivity}$$

and,

$$Minimum\ exposure\ detection\left(Roentgen\right) = \frac{512\,R}{sensitivity}$$

Here the factor 512 Roentgen is Minimum Detectable Activity (MDA). It is defined as the activity which will result in a count rate significantly different from background for a given time.

Therefore,

$$MDA = \frac{M_{min.sensitivity} + N_{max.sensitivity}}{2}$$

Where M & N is twice of a standard deviation of an average TL counts of completely annealed stone.

The TL Integral counts of the samples for background and the radiation exposure are shown in Table 1. The glow curves of the samples for background and the radiation exposures measured using the Nucleonix TLD reader are shown in Fig.1 to Fig.3 for three important samples (S-2, S-7, S-15).

Table 1: TL Analysis of Himalayan Stones for Nuclear Radiation Measurement

TL Analysis of Himalayan Stones for Nuclear Radiation Measurement									
Sample ID	Background (Natural) TL Integral count (AU)	TL Integral Counts (300 R)			Average TL Counts	Net TL Integral Counts for 300 R	Sensitivity (AU/R/50mg) A	Natural Radiation Exposure (Roentgen)	Minimum Exposure Detection (Roentgen)-512/A
		Reading-1	**Reading-2**	**Reading-3**					
S-2	74566.00	80893.00	81991.00	81245.00	81376.33	6810.33	22.70	3284.69	22.55
S-6	7413.00	12532.00	19437.00	12250.00	14739.67	7326.67	24.42	303.54	20.96
S-7	16895.00	19551.00	18655.00	19510.00	19238.67	2343.67	7.81	2162.64	65.54
S-8	106888.00	108895.00	105919.00	112536.00	109116.67	2228.67	7.43	14388.15	68.92
S-11	49650.00	49318.00	51143.00	51679.00	50713.33	1063.33	3.54	14007.84	144.445
S-12	22294.00	26511.00	23357.00	24348.00	24738.67	2444.67	8.15	2735.83	62.83
S-14	4358.00	10038.00	8992.00	8811.00	9280.33	4922.33	16.41	265.61	31.20
S-15	24406.00	278444.00	286307.00	286625.00	283792.00	39786.00	132.62	1839.89	3.86
S-17	91321.00	106655.00	114006.00	110633.00	110431.33	19110.33	63.70	1433.59	8.04
S-18	3062.00	3853.00	2893.00	3534.00	3426.67	364.67	1.22	2519.01	421.121
S-19	230771.00	248305.00	236639.00	241641.00	242195.00	11424.00	38.08	6060.16	13.45
S-20	24187.00	23043.00	24063.00	30349.00	25818.33	1631.33	5.44	4447.96	94.16
S-21	26338.00	27972.00	33118.00	30383.00	30491.00	4153.00	13.84	1902.58	36.99
S-22	56613.00	61617.00	67391.00	65033.00	64680.33	8067.33	26.89	2105.27	19.04
S-26	24720.00	29734.00	26651.00	28033.00	28139.33	3419.33	11.40	2168.84	44.92

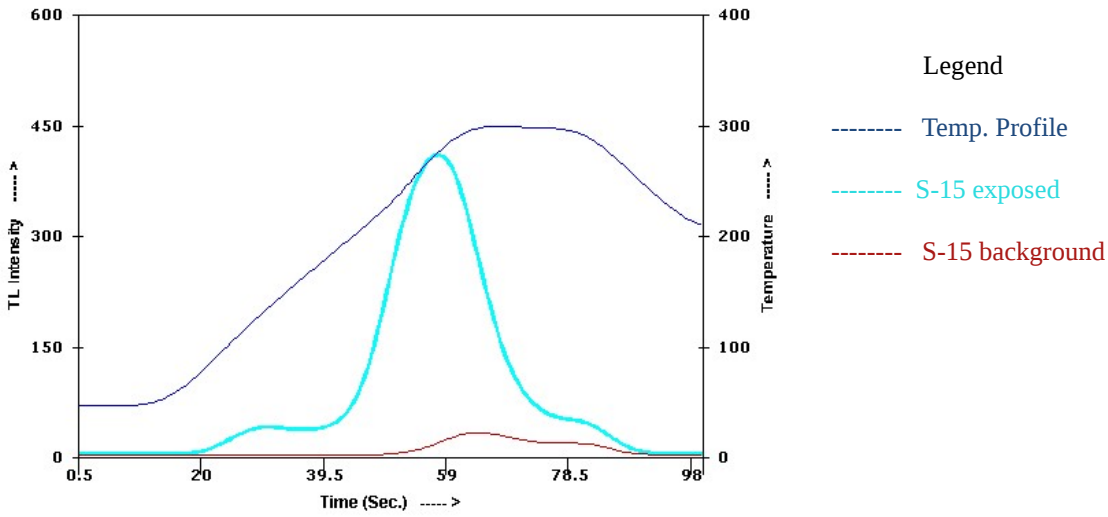

Fig.1: Graph showing Glow Curve of Sample S-15 (Exposed and Background)

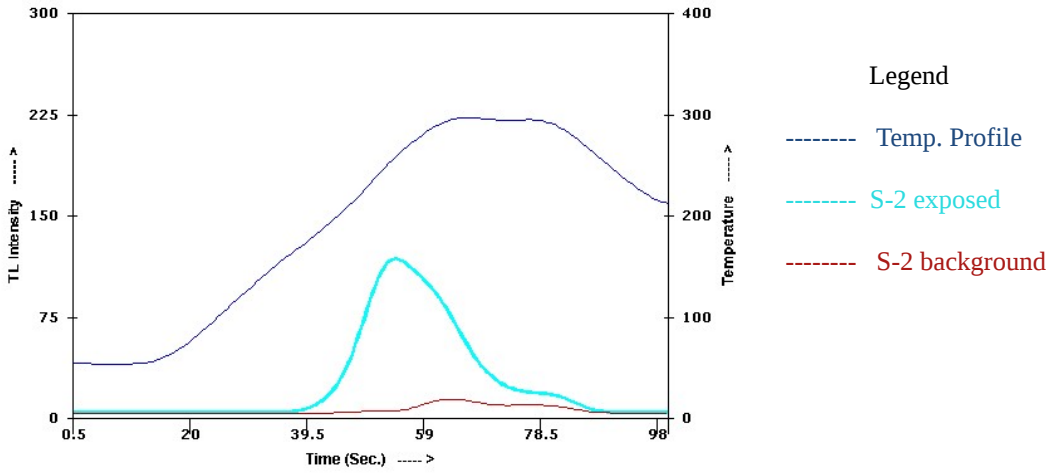

Fig.2: Graph Showing Glow Curve of Sample S-2 (Exposed and Background)

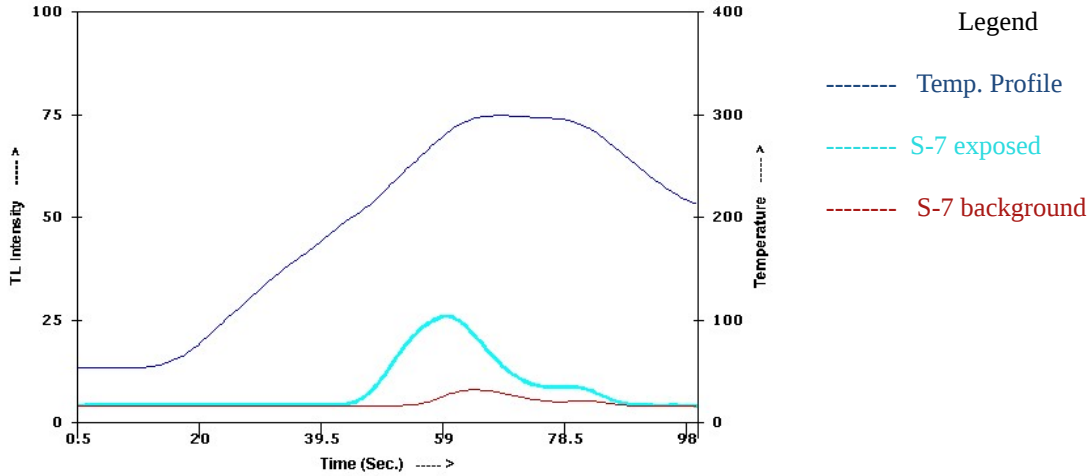

Fig.3: Graph Showing Glow Curve of Sample S-7 (Exposed and Background)

3. RESULTS & DISCUSSIONS:

3.1. TL Sensitivity: Out of 26 studied Himalayan Stones for TL, 15 samples have shown significant TL sensitivity to be used for ionizing radiation measurement in various applications. The variation in TL sensitivity is graphically shown in Fig.4. The TL sensitivity of these 15 samples is found to vary from 1.2 to 132.6 AU/R/50mg, with a minimum radiation detection level from 3.86 to 421.21 R of gamma radiation.

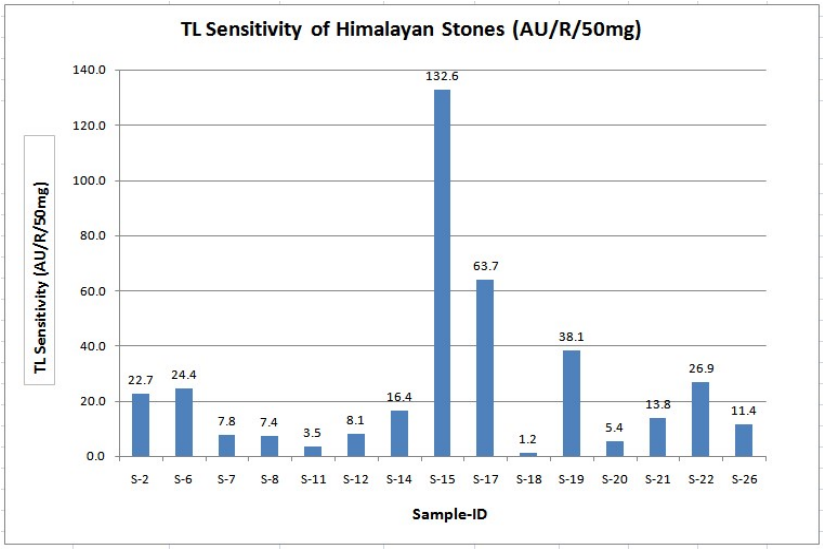

Fig. 4: TL Sensitivity in terms of AU/R/50mg

3.2: Estimation of Natural Radiation Exposure in Himalayan Stones: All materials of the universe are being continuously irradiated form the natural radiation (cosmogenic and terrestrial). TL analysis of the raw stone samples (without annealing) can give approximate estimate of the natural ionizing radiation, which a typical stone has received through exposure to the environment. This has also been explored in this study and the exposure levels in these stones have been found to be in the range of 304 to 14388 R. These estimations have been graphically represented in Fig. 5.

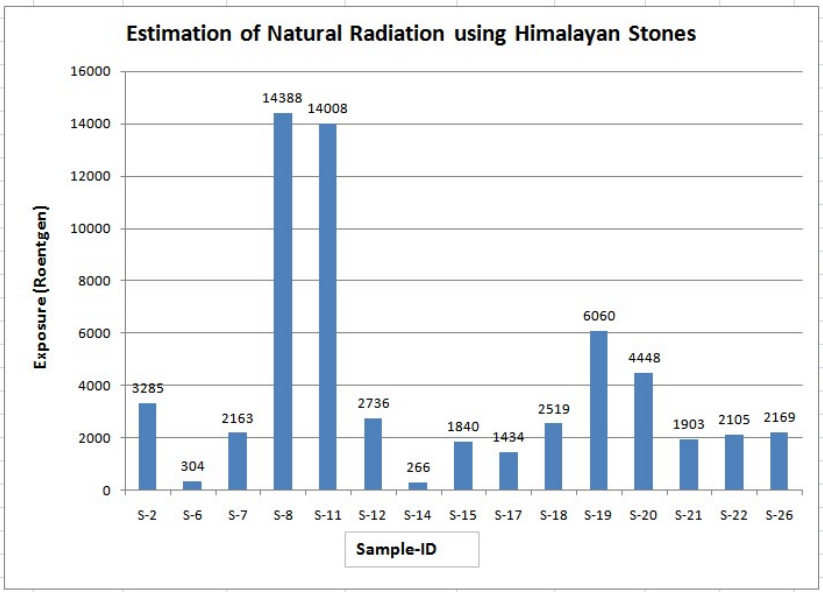

Fig. 5: Estimate of Natural Radiation Exposure

4. CONCLUSIONS:

The TL analysis of the stone samples irradiated by gamma dose has enough TL sensitivity which can be used for ionizing radiation measurement in case of radiological / nuclear emergencies and also medical applications. The glow peak of most of the stones is found below 300 ^{0}C, which is suitable for TL radiation dosimetry also.

5. FUTURE PROSPECTS:

Higher sensitive stones can be further studied for additional radiation dosimetric parameters such as; linearity, reproducibility, repeatability and TL fading etc. for establishing them as TL material for radiation dosimetry.

6. ACKNOWLEDGEMENTS:

Manish Joshi is thankful to Defence Laboratory, DRDO, Jodhpur for support to carry this work. He expresses his gratitude to supervisor Dr. Pradeep Narayan (Scientist E) Defence Laboratory, Jodhpur and co-supervisor Dr.(Mrs.) Sumita Srivastava (Associate professor of physics) of Pt. L.M.S. Government Post Graduate College, Rishikesh for their support and suggestions during preparation of manuscript.

References:

1. Dr. Vij and N. Singh, Luminescence and realated properties of II-VI semiconductors; Classes of Luminescence; ISBN 1-56072-433-1
2. Dr. Hitesh Mandavia, 2015, Thermoluminescence study of ceramic tiles materials; ISBN 978-9384044-78-7.

STUDENT JOURNAL OF PHYSICS

Volume 7 **Number 2** **Apr - Jun 2018**

CONTENTS

ARTICLES